Bull. Mater. Sci., Vol. 35, No. 4, August 2012, pp. 519–527. © Indian Academy of Sciences.

Spherical and rod-like $Gd_2O_3:Eu^{3+}$ nanophosphors—Structural and luminescent properties

N DHANANJAYA[1,2], H NAGABHUSHANA[3,*], B M NAGABHUSHANA[4], B RUDRASWAMY[1], C SHIVAKUMARA[5] and R P S CHAKRADHAR[6]

[1]Department of Physics, J.B. Campus, Bangalore University, Bangalore 560 056, India
[2]Department of Physics, B.M.S. Institute of Technology, Bangalore 560 064, India
[3]Department of PG studies & Research in Physics, University College of Science, Tumkur University, Tumkur 572 103, India
[4]Department of Chemistry, M.S. Ramaiah Institute of Technology, Bangalore 560 054, India
[5]Solid State and Structural Chemistry Unit, Indian Institute of Science, Bangalore 560 012, India
[6]Glass Technology Lab, Central Glass and Ceramic Research Institute (CSIR), Kolkata 700 032, India

MS received 8 March 2011; revised 20 June 2011

Abstract. **A comparative study of spherical and rod-like nanocrystalline $Gd_2O_3:Eu^{3+}$ ($Gd_{1.92}Eu_{0.08}O_3$) red phosphors prepared by solution combustion and hydrothermal methods have been reported. Powder X-ray diffraction (PXRD) results confirm the as-formed product in combustion method showing mixed phase of monoclinic and cubic of $Gd_2O_3:Eu^{3+}$. Upon calcinations at 800°C for 3 h, dominant cubic phase was achieved. The as-formed precursor hydrothermal product shows hexagonal $Gd(OH)_3:Eu^{3+}$ phase and it converts to pure cubic phase of $Gd_2O_3:Eu^{3+}$ on calcination at 600°C for 3 h. TEM micrographs of hydrothermally prepared cubic $Gd_2O_3:Eu^{3+}$ phase shows nanorods with a diameter of 15 nm and length varying from 50 to 150 nm, whereas combustion product shows the particles to be of irregular shape, with different sizes in the range 50–250 nm. Dominant red emission (612 nm) was observed in cubic $Gd_2O_3:Eu^{3+}$ which has been assigned to $^5D_0 \rightarrow {}^7F_2$ transition. However, in hexagonal $Gd(OH)_3:Eu^{3+}$, emission peaks at 614 and 621 nm were observed. The strong red emission of cubic $Gd_2O_3:Eu^{3+}$ nanophosphors by hydrothermal method are promising for high performance display materials. The variation in optical energy bandgap (E_g) was noticed in as-formed and heat treated systems in both the techniques. This is due to more ordered structure in heat treated samples and reduction in structural defects.**

Keywords. **Red phosphor; combustion; hydrothermal; photoluminescence; optical.**

1. Introduction

Rare earth oxides (RE_2O_3) are the most stable rare earth compounds, in which the rare earth ions hold typically a trivalent state (Xu *et al* 2002). Because of their optical, electronic, and chemical properties resulting from their $4f$ electrons, rare earth oxides have been widely used in the fields of luminescent devices, optical transmission, biochemical probes, medical diagnosis and so forth (Tang *et al* 2003). It is known that nanostructured rare earth oxides exhibit improved luminescent properties. In recent years, controlled synthesis of well-defined inorganic nanophosphors has been a focus of worldwide research due to various potential applications. Therefore, dramatic efforts have been made to develop new methods for the synthesis of high-quality inorganic nanostructures in different systems. From the perspective of application, nanomaterials are not only synthesized in large quantities with a desired composition, reproducible size, shape, and structure but also are prepared and assembled using simplicity, low costs, ease of scale-up and relative greenness (aqueous solution) which constitute the key trains of this method. Therefore, the development of more controlled methods for creating such novel architectures will be of general interest.

An improved performance of displays and lamps requires high quality of phosphors for sufficient brightness and long term stability. To enhance the luminescent characteristics of the phosphors, extensive research has been carried out on rare earth-activated oxide-based phosphors in various methods (Gu *et al* 2008). Due to their good luminescent characteristics, stability in high vacuum and absence of corrosive gas emission under electron bombardment when compared to currently used sulfide-based phosphors oxide-based phosphors are likely to emerge as the potential choice for the field emission display (FED) phosphors.

As a part of our programme on nanomaterials, here we report a comparative study of spherical and rod-like nanocrystalline $Gd_2O_3:Eu^{3+}$ ($Gd_{1.92}Eu_{0.08}O_3$; 8 mol %) red phosphors prepared by solution combustion and hydrothermal methods, respectively. The luminescence of Eu^{3+} doped is particularly interesting because its major emission band is centred near 612 nm (red) while red is one of the three

*Author for correspondence (bhushanvlc@gmail.com)

primary colours (red, blue and green) from which a wide spectrum of colours can be generated by appropriate mixing, including white. For this reason Eu^{3+} has been thoroughly investigated as a luminescent activator in many host lattices (Nagabhushana 2008). Gadolinium oxide (Gd_2O_3) is a promising host matrix for doping with Eu^{3+} because of its good chemical durability, thermal stability and low phonon energy. Literature reveals that a very limited work has been carried out on Gd_2O_3:Eu^{3+} system prepared via combustion and hydrothermal methods, hence in this study we demonstrate low temperature solution combustion and surfactant free hydrothermal methods to prepare Gd_2O_3:Eu^{3+} nanophosphor and evaluate their structural and photoluminescent properties.

2. Experimental

2.1 *Synthesis of Gd_2O_3:Eu^{3+} nanophosphors*

In the combustion and hydrothermal synthesis all the starting chemical reagents used were obtained from commercial sources. In a typical combustion synthesis, stoichiometric amounts of Gd_2O_3 and Eu_2O_3 were dissolved in 1:1 HNO_3. A clear solution was obtained by uniform stirring and thereafter, the solution was heated on a sand bath to evaporate excess HNO_3. The oxalyl dihydrazide ($C_2H_6N_4O_2$; ODH) was added as a fuel and mixed with a magnetic stirrer for 10 min. ODH was used as a fuel in the combustion synthesis which was prepared in our laboratory by the reaction of diethyl oxalate and hydrazine hydrate as described in the literature (Nagabhushana 2008). The petri dish containing the redox mixture was placed in a pre-heated muffle furnace maintained at 400 ± 10°C. The reaction mixture initially undergoes thermal dehydration followed by ignition with liberation of large amounts of gaseous products such as oxides of nitrogen and carbon. Finally, a voluminous and foamy whitish product was obtained.

In a typical hydrothermal synthesis, stoichiometric amounts of Gd_2O_3 and Eu_2O_3 were dissolved in 1:1 HNO_3. A clear solution was obtained by uniform stirring and thereafter, the solution was heated on a sand bath to evaporate excess HNO_3. The aqueous KOH (1·0 N) solution was added into the above solution until pH of solution was adjusted to be around 12. The resulting colloidal mixture was put into a Teflon-lined stainless steel autoclave with a capacity of

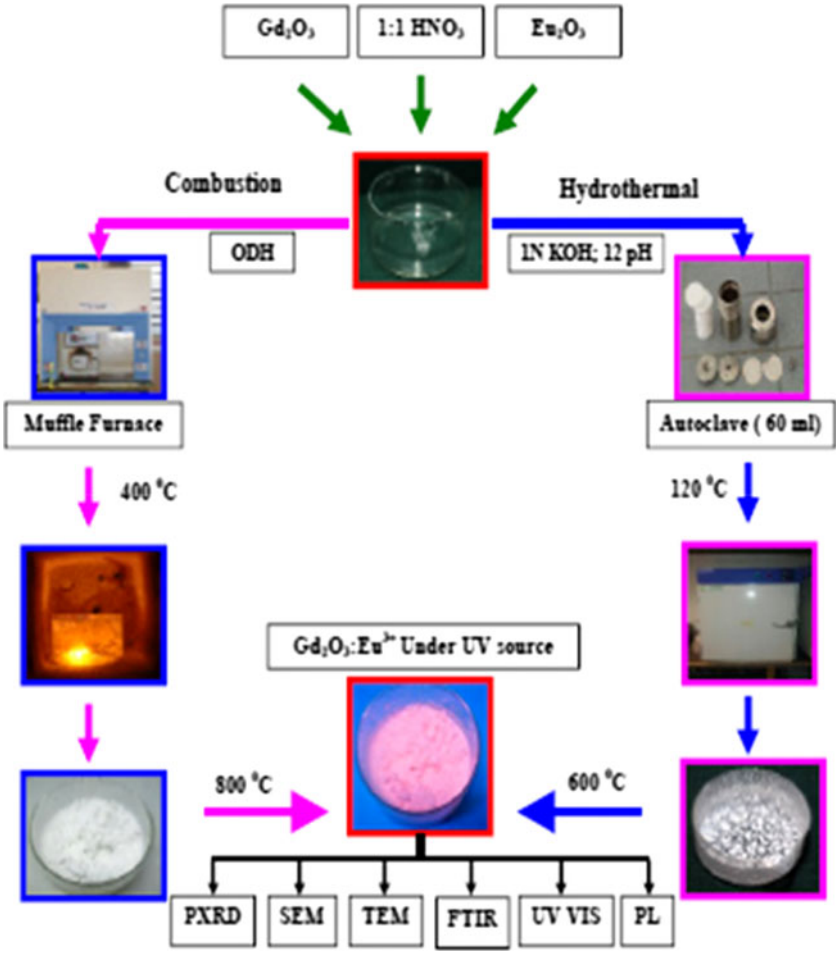

Figure 1. Flow chart for synthesis of Gd_2O_3:Eu^{3+} nanophosphors by combustion and hydrothermal methods.

120 mL at room temperature (*RT*). The autoclave was then sealed and maintained at 145°C for 20 h and thereafter, naturally cooled to room temperature. A white solid product of $Gd(OH)_3$:Eu was collected by filtration and washed several times with distilled water and ethyl alcohol and then dried at 100°C. Subsequent dehydration of $Gd(OH)_3$:Eu^{3+} by heat treatment at 600°C for 3 h results in cubic Gd_2O_3:Eu^{3+}. The flow chart for the synthesis Gd_2O_3:Eu^{3+} phosphor by combustion and hydrothermal methods is shown in figure 1.

2.2 *Instruments used*

The phase purity of the nanophosphors is examined by powder X-ray diffractometer (PXRD) (PANalytical X′Pert Pro) using CuKα radiation (λ = 1·541 Å) with a nickel filter to estimate crystallinity of the phases. The surface morphology of the samples has been examined using scanning electron microscopy (JEOL JSM 840A) by sputtering technique with gold as covering contrast material. Transmission electron microscopy (TEM) analysis was performed on a Hitachi H-8100 (accelerating voltage up to 200 kV, LaB_6 filament) instrument. The UV-Vis spectra were recorded on a UV-3101 Shimadzu spectrometer. The photoluminescence studies were carried out using a Perkin–Elmer LS-55 luminescence spectrophotometer equipped with Xe lamp (excitation wavelength 250 nm).

3. Results and discussion

Figure 2 shows the powder X-ray diffraction patterns of $Gd_{1·92}Eu_{0·08}O_3$ nanophorsphors prepared by combustion and hydrothermal techniques. In combustion process (figures 2 (a) and (b)), PXRD of as-formed product shows mixed phase (monoclinic and cubic) (JCPDS card no.43-1015 and 86-2477). After calcination at 800°C for 3 h, the dominant cubic Gd_2O_3:Eu^{3+} phase was observed (JCPDS card no. 86-2477) along with weak monoclinic phase. The relative broad peaks suggest the nanocrystalline nature of the rare earth oxide. No crystalline impurity apart from rare earth oxide can be determined from PXRD analysis. However, the as-formed precursor product in the hydrothermal method (figure 2 (c)) readily indicated as hexagonal $Gd(OH)_3$:Eu^{3+}

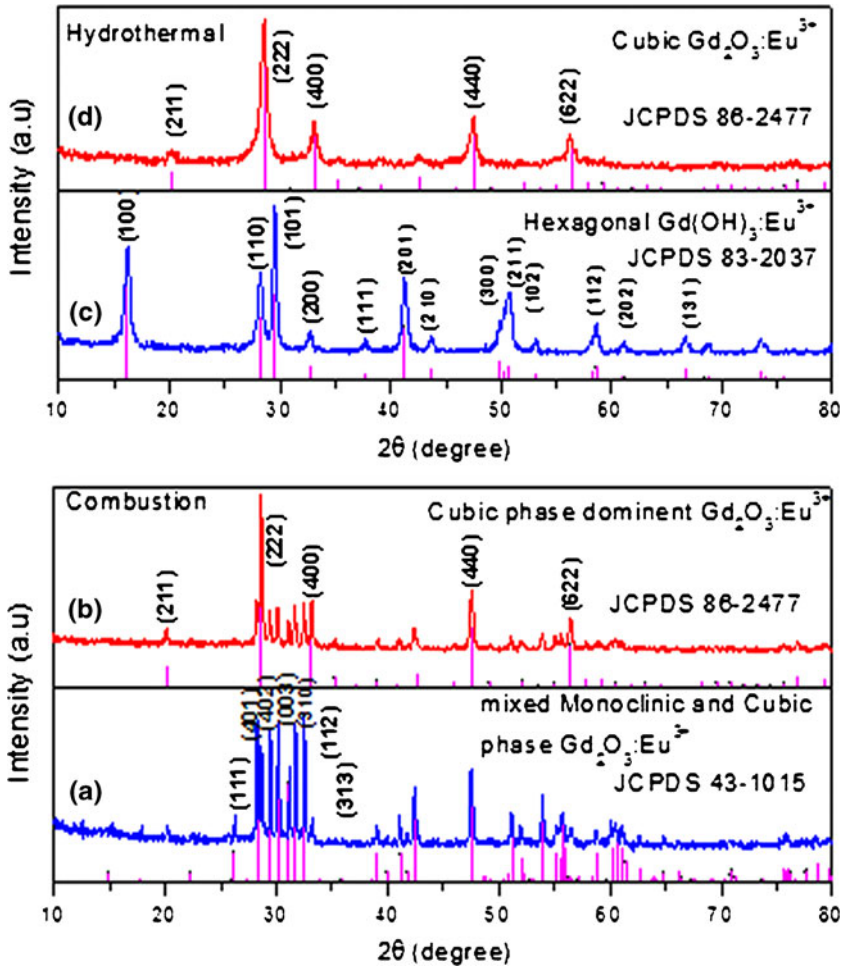

Figure 2. PXRD patterns of Gd_2O_3:Eu^{3+} combustion synthesized (**a**) as formed, (**b**) calcinated at 800°C and hydrothermally synthesized (**c**) as formed and (**d**) calcinated at 600°C for 3 h.

with space group $P\ 63/m$, and lattice constants $a = b = 0{\cdot}63$ nm and $c = 0{\cdot}36$ nm (JCPDS card No. 83-2037) (Chang *et al* 2005). When product was calcined at 600°C for 3 h, hexagonal $Gd(OH)_3:Eu^{3+}$ phase was converted into pure cubic $Gd_2O_3:Eu^{3+}$ (figure 2 (d)) phase (JCPDS card no. 86-2477 with space group *Ia*-3) without achieving intermediate monoclinic phase, $GdOOH:Eu^{3+}$.

The lattice constants of the cubic $Gd_2O_3:Eu^{3+}$ were calculated according to the equation

$$1/d^2 = \left(h^2 + k^2 + l^2\right)/a^2, \tag{1}$$

where d is the interplanar distance, h, k, l are the crystal indices (Miller indices), and a being lattice constant. On the basis of the (2 2 2) crystal planes ($d = 3{\cdot}1179$ Å in figure 2b, $d = 3{\cdot}1289$ Å in figure 2 d), the lattice constant is $a = 10{\cdot}8007$ Å and $10{\cdot}8388$ Å for combustion and hydrothermal cubic $Gd_2O_3:Eu^{3+}$, respectively, which is well compatible with the literature value of $a = 10{\cdot}809(9)$ Å (JCPDS No. 86-2477) and are tabulated in table 1. These values are in good agreement with those observed in the literature (Jis *et al* 2009; Li *et al* 2010).

The crystallite size was calculated from the broad PXRD peaks using the Scherrer's equation (Klug and Alexander 1954)

$$d = \frac{0{\cdot}9\,\lambda}{\beta\,\cos\theta}, \tag{2}$$

where d is the average grain size of the crystallites, λ the incident wavelength, θ the Bragg angle and β the diffracted full-width at half-maximum (FWHM) in radians caused by the crystallites. The mean crystallite size is calculated and tabulated in table 1.

The grain size was also calculated from the powder X-ray diffraction line broadening (B) using the analysis described by Williamson and Hall (W–H) (1953) method.

$$B\cos\theta = \varepsilon\,(4\sin\theta) + \frac{\lambda}{D}, \tag{3}$$

where B (FWHM in radian) is measured for different XRD lines corresponding to different planes, ε the strain developed and D the grain size. The equation represents a straight line between 4 sin θ (X-axis) and B cos θ (Y-axis). The slope of line gives the strain (ε) and intercept (λ/D) of this line on the Y-axis gives grain size (D).

The grain size determined from W–H formula is slightly higher than those calculated using Scherrer's formula (table 1). The small increase in the values is due to the fact that in Scherrer's formula strain component is assumed to be zero and observed broadening of diffraction peak is considered as a result of reducing grain size only.

In order to obtain an insight information about surface morphology and particle size of the samples, SEM and TEM analyses were performed. Figures 3 (a) and 4 (a) show SEM and TEM images of the as-formed $Gd_2O_3:Eu^{3+}$ phosphor derived from combustion method. The product is agglomerated from few μm to a few tens of μm, fluffy and porous in nature. However, when phosphor was calcined at 800°C

Table 1. Various parameters of $Gd_2O_3:Eu^{3+}$ nanophosphor.

Preparation method	Phase and sample	Particle size (nm)		Particle size by TEM (nm)	Estimated lattice parameter (Å)	Lattice parameter (JCPDS) (Å)	Energy gap (eV)
		Scherrer's equation (d)	W–H method (D)				
Combustion	As-formed (C & M) $Gd_2O_3:Eu^{3+}$	48–76	50–82	50–250	$a = 14{\cdot}081$* $b = 3{\cdot}556$ $c = 8{\cdot}779$	$a = 14{\cdot}061$ $b = 3{\cdot}566$ $c = 8{\cdot}76$	5·28
Hydrothermal	Calcined at 800°C (C ; with small M) $Gd_2O_3:Eu^{3+}$	34–50	46–64	–	$a = 10{\cdot}8007$	$a = 10{\cdot}809(9)$	5·41
	As-formed (H)$Gd(OH)_3:Eu^{3+}$	–	–	Diameter = 15 Length = 50–150	$a = b = 6{\cdot}300$* $c = 3{\cdot}600$	$a = b = 6{\cdot}329(2)$ $c = 3{\cdot}631(1)$	5·64
	Calcined at 600°C (C) $Gd_2O_3:Eu^{3+}$	–	–	–	$a = 10{\cdot}8388$	$a = 10{\cdot}809(9)$	5·43

C, cubic phase; M, monoclinic phase; H, hexagonal phase; *reported in Dhananjaya *et al* (2010, 2011b).

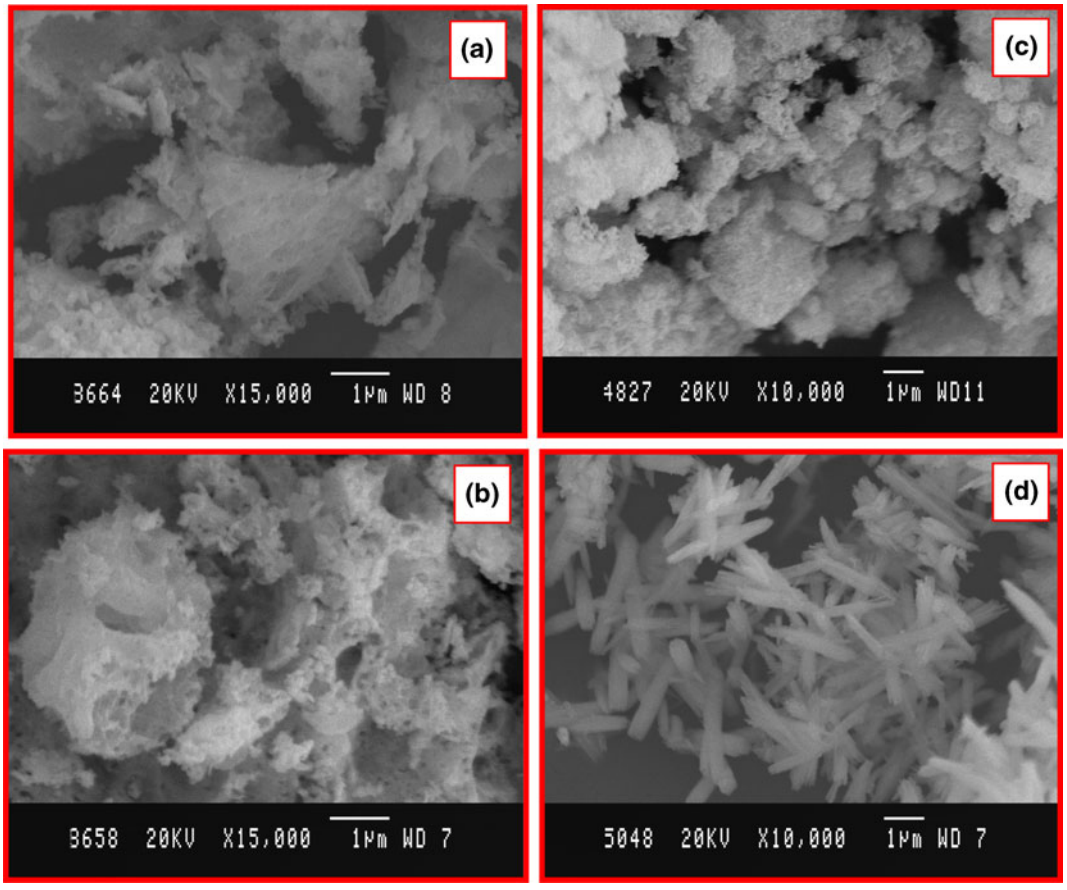

Figure 3. SEM profiles of Gd_2O_3:Eu^{3+} combustion synthesized **a**. as formed, **b**. calcinated at 800°C and hydrothermally synthesized **c**. as formed and **d**. calcinated at 600°C for 3 h.

for 3 h, the agglomeration was reduced with increase in grain growth (figure 3 (b)). The agglomeration of particles is usually explained as a common way to minimize their surface free energy. The large voids and porous product in the combustion derived phosphor are due to large amount of gases such as NO_2 and CO_2 produced during combustion method (Dhananjaya *et al* 2010). TEM pictures of combustion product (figure 4 (a)) show the particles to be irregular in shape, with different sizes in the range 50–250 nm. The particle size obtained from TEM is in good agreement with that of Scherrer's equation (Klug and Alexander 1954). The spotty angular rings in the SAED patterns further indicate nanosized crystalline nature of the Gd_2O_3:Eu^{3+} (figure 4 (b)). SEM micrographs of hydrothermally synthesized as-formed ($Gd(OH)_3$:Eu^{3+}) and calcined at 600°C for 3 h (Gd_2O_3:Eu^{3+}) are shown in figures 3 (c) and (d), respectively. The as-formed product was agglomerated with irregularly shaped rods (figure 3 (c)). However, upon calcination at 600°C for 3 h, the agglomeration of rods was reduced and overlapping of the rods with tapered ends was also observed. Typical TEM image of the hydrothermally synthesized hexagonal $Gd(OH)_3$:Eu^{3+} (figure 4 (c)) exhibits nanorods which are relatively straight, smooth and uniform in diameter, ∼15 nm and length varying from 50–150 nm. Figure 4 (d) shows the corresponding selected area diffraction (SAED) pattern of the well crystallized nanorods.

Figure 5 shows FT–IR spectra of as-formed and calcined $Gd_{1.92}Eu_{0.08}O_3$ phosphors obtained from combustion and hydrothermal methods. All the samples show absorption peaks of H_2O near 3410 cm^{-1}. The as-formed product obtained from combustion method shows (figure 5 (a)) a weak absorption peak in the range 1400–1700 cm^{-1} which are due to hydroxyl carbonate or carbonate groups. The formation of these phases might be due to the reaction between Gd_2O_3 and CO_2 produced during combustion reaction. Upon calcination at 800°C for 3 h (figure 5 (b)), the carbonate or hydroxy carbonate peaks weakened and the stretching vibrations of the Gd–O bonds at 400 and 540 cm^{-1} became stronger. The hydrothermally derived as-formed product shows (figure 5 (c)) distinct–OH peaks at 703 and 3616 cm^{-1} along with peaks of Gd–O. Upon calcinations at 600°C for 3 h, the FTIR spectrum shows Gd–O absorption bands at 400 and 540 cm^{-1} (figure 5 (d)).

The UV-Vis absorbance spectra of combustion and hydrothermal synthesized $Gd_{1.92}Eu_{0.08}O_3$ phosphors are shown in figure 6. A broad absorption peak was observed at 286 nm in combustion derived products whereas sharp

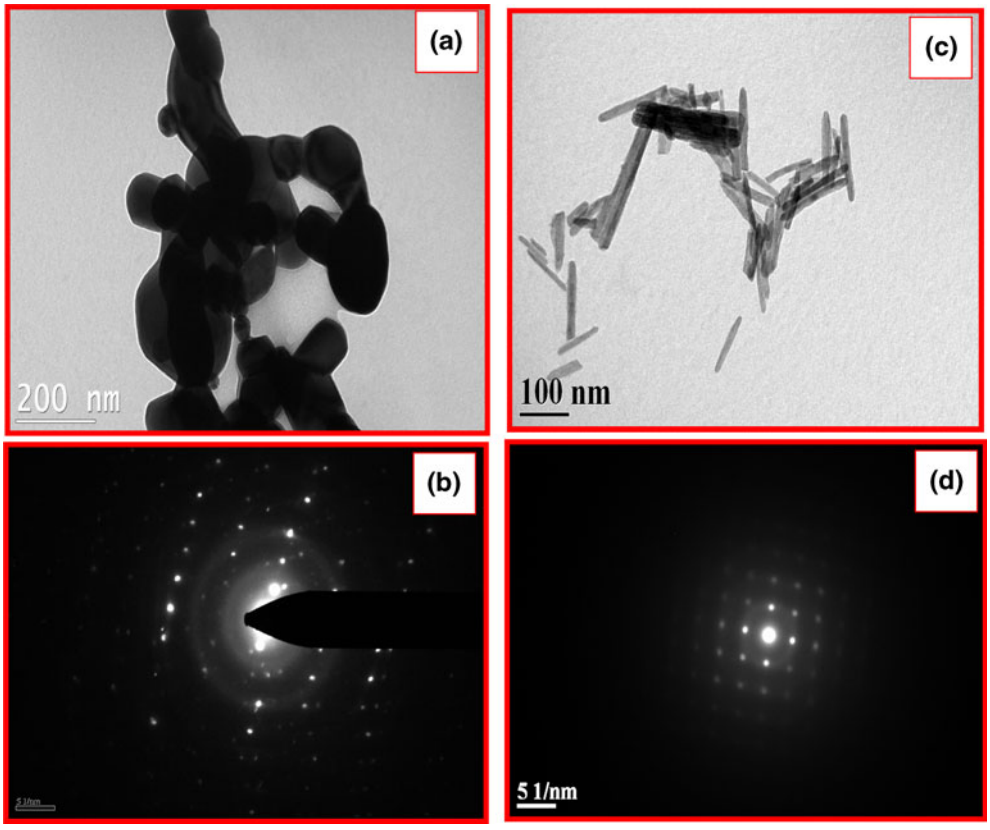

Figure 4. TEM images of $Gd_2O_3:Eu^{3+}$ (**a**) combustion, (**b**) hydrothermal, (**c**) SAED pattern of combustion and (**d**) SAED pattern of hydrothermal.

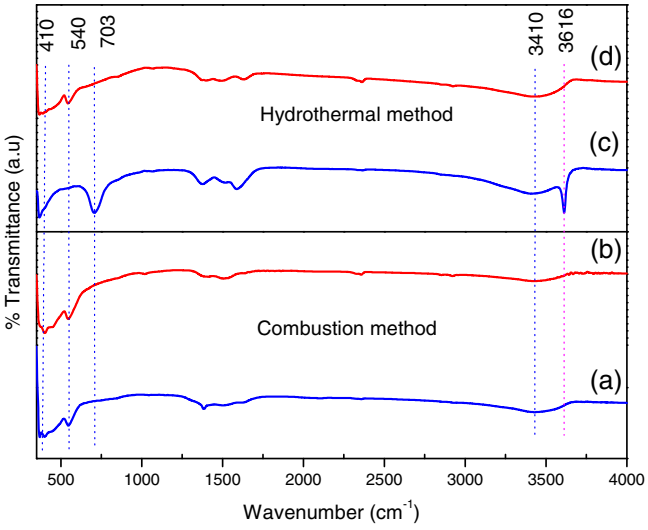

Figure 5. FTIR spectrum of $Gd_2O_3:Eu^{3+}$ combustion synthesized (**a**) as formed, (**b**) calcinated at 800°C and hydrothermally synthesized, (**c**) as formed and (**d**) calcinated at 600°C for 3 h.

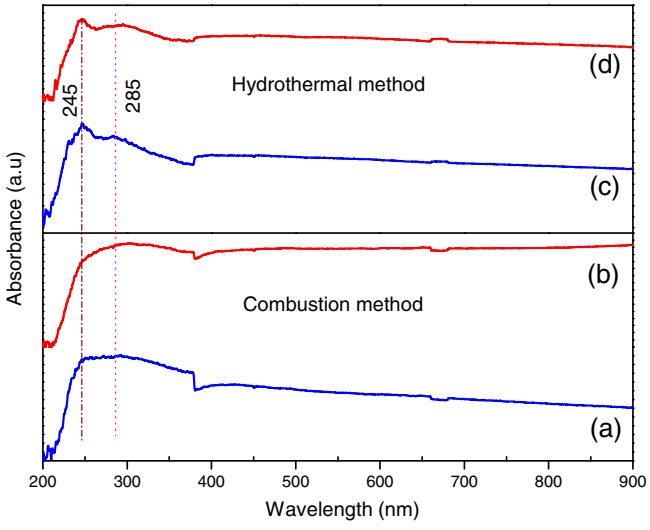

Figure 6. UV-Vis spectrum of $Gd_2O_3:Eu^{3+}$ combustion synthesized (**a**) as formed, (**b**) calcinated at 800°C and hydrothermally synthesized, (**c**) as formed and (**d**) calcinated at 600°C for 3 h.

absorption peaks at 245 nm were observed in both as-formed (hexagonal $Gd(OH)_3:Eu^{3+}$) and calcined (cubic $Gd_2O_3:Eu^{3+}$) hydrothermal products. A broad and weak peak at 285 nm is also observed in hexagonal phase, which slightly (12 nm) shifted to higher wavelength in cubic phase. The maximum absorption can arise due to transition between

valence band to conduction band (Pan *et al* 2004). The weak absorption in the UV-Visible region is expected to arise from transitions inverting extrinsic states such as surface traps or defect states or impurities (Cao *et al* 2004).

The optical bandgap energy (E_g) of samples was estimated by Wood and Tauc (1972) relation and is shown in figure 7. The optical bandgap is associated with absorbance and photon energy by the following relation

$$\alpha h\gamma \propto \left(h\gamma - E_g\right)^n, \tag{4}$$

where α is the absorbance, h the Planck constant, γ the frequency, E_g the optical bandgap and k a constant associated to the different types of electronic transitions ($n = 1/2$, 2, 3/2 or 3 for direct allowed, indirect allowed, direct forbidden and indirect forbidden transitions, respectively). According to the literature (Liu *et al* 2008), the oxides are characterized by an indirect allowed electronic transition and hence, $n = 2$ value was used as standard in (4). Thus, the E_g values have been evaluated by extrapolating the linear portion of the curve or tail $[(\alpha h\nu)^{1/n} = 0]$ in the UV–Vis absorbance spectra. A plausible explanation for the variation observed in the E_g values can be related to the degree of structural order–disorder in the lattice which is able to change the intermediate energy level distribution within the bandgap (Dhananjaya *et al* 2011a).

The as-formed precursor obtained by hydrothermal method is hexagonal $Gd(OH)_3$:Eu^{3+} phase with a high degree of structural defects. Upon calcination, $Gd(OH)_3$:Eu^{3+} undergoes decomposition to yield $Gd(OH)_3$:Eu^{3+}:

$$\underset{\text{Hexagonal phase}}{2Gd(OH)_3:Eu^{3+}} \xrightarrow{600^\circ C \text{ for } 3h} \underset{\text{Cubic phase}}{Gd_2O_3:Eu^{3+}}, \tag{5}$$

The cubic Gd_2O_3:Eu^{3+} has more ordered structure with fewer defects. Consequencely intermediate energy levels (deep and shallow holes) are minimized within the optical bandgap and E_g increases.

Table 1 shows particle size, lattice parameters and optical bandgap energy (E_g) values of Gd_2O_3:Eu^{3+} nanophosphors obtained by combustion and hydrothermal techniques along with literature values. E_g values mainly depend on the preparation methods and experimental conditions (heat treatment and processing time). In particular, these key factors can favour or inhibit the formation of structural defects, which are able to control the degree of structural order–disorder of the material and consequently the number of intermediate energy levels within the bandgap.

Figures 8 (a) and (b) show the excitation spectrum of $Gd_{1.92}Eu_{0.08}O_3$ phosphors prepared by combustion and hydrothermal methods, respectively. The peak at 235 nm originates from the emission of Gd_2O_3 with lattice (HL), the peak at 254 nm is due to charge transfer (CT) peak which attributes to the transition from O^{2-} $2p$ state to Eu^{3+} $4f$ state (Liu *et al* 2007). The other peaks observed at 267–338 nm are related to internal Gd^{3+} ion f–f transitions (Pires *et al* 2001; Li *et al* 2010).

The photoluminescence spectrum of combustion synthesized Gd_2O_3:Eu^{3+} is shown in figure 9 (a, b). In mixed phase of monoclinic and cubic, Gd_2O_3:Eu^{3+} phosphor exhibits weak emission peaks at 612 and 623 nm. However, in cubic, Gd_2O_3:Eu^{3+} (calcined) exhibits dominant red emission peaks at 610 and 623 nm. Figure 9 (c) shows PL emission spectrum of hydrothermally derived hexagonal $Gd(OH)_3$:Eu^{3+} phosphor excited under 254 nm wavelength. This phase shows weak and broad emission peaks at $\sim$ 465, 575, 614 and 621 nm. The emission lines with peaks at $\sim$ 614 and 621 nm observed for the $^5D_0 \rightarrow {}^7F_2$ transition is consistent with the hexagonal $Gd(OH)_3$:Eu^{3+} (Louis *et al*

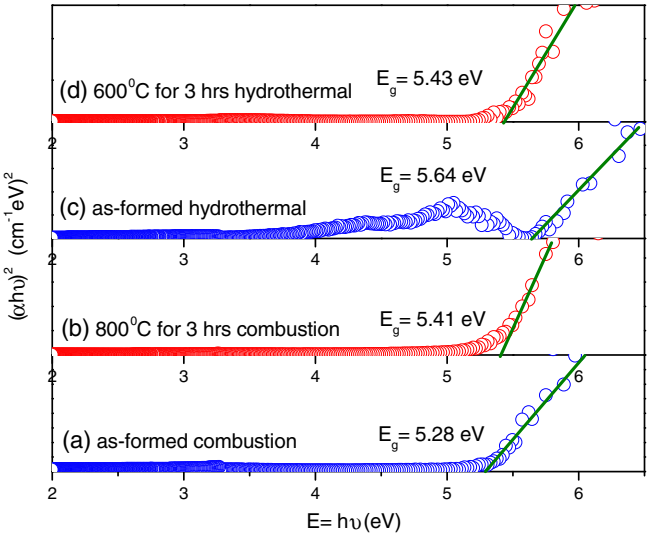

Figure 7. Energy bandgap of Gd_2O_3:Eu^{3+} combustion synthesized (**a**) as formed, (**b**) calcinated at 800°C and hydrothermally synthesized, (**c**) as formed and (**d**) calcinated at 600°C for 3 h.

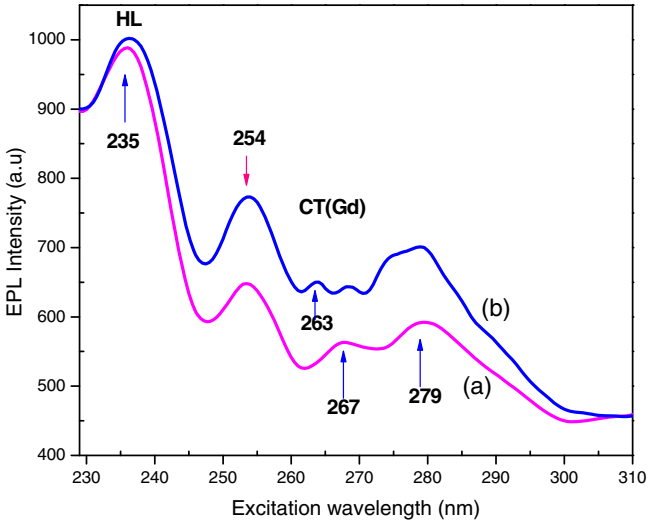

Figure 8. PL excitation spectra of Gd_2O_3:Eu^{3+} (**a**) combustion method and (**b**) hydrothermal method.

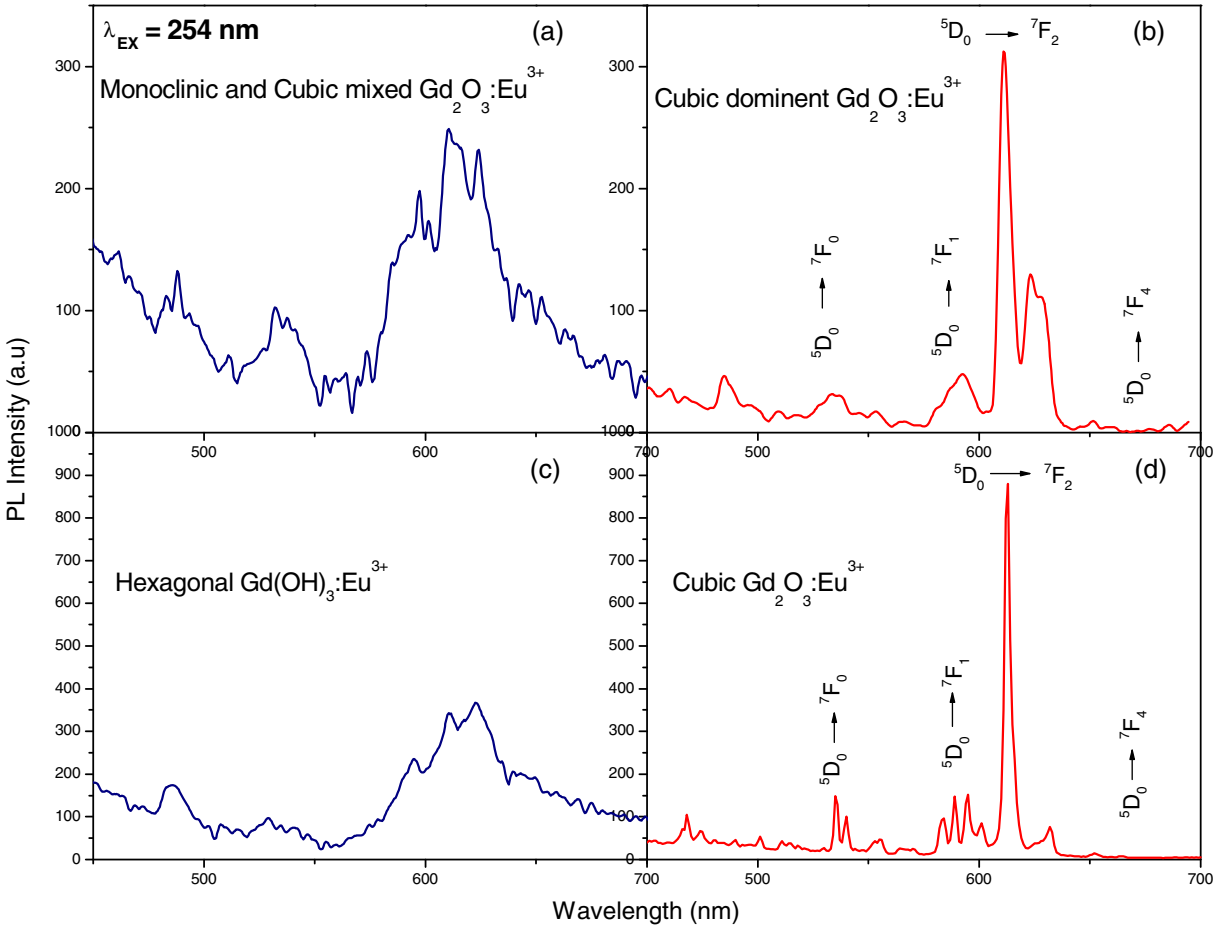

Figure 9. PL emission spectrum of Gd_2O_3:Eu^{3+} combustion synthesized (**a**) as formed, (**b**) calcinated at 800°C and hydrothermally synthesized, (**c**) as formed and (**d**) calcinated at 600°C for 3 h.

2003). Figure 9 (d) shows PL spectrum of hydrothermally derived cubic Gd_2O_3:Eu^{3+} excited under same 254 nm wavelength. The spectrum consists of a series of emission lines at ~534, 539, 554, 583, 589, 594, 600, 613, and 632 nm, respectively. These emission lines correspond to transition from $^5D_0 \rightarrow {}^7F_J$ ($J = 0, 1, 2, 3, 4$) manifolds of Eu^{3+}. The $^5D_0 \rightarrow {}^7F_J$ emission is very sensitive to the crystal field around Eu^{3+} sites. The Eu^{3+}, $^5D_0 \rightarrow {}^7F_{1,3}$ is an allowed magnetic dipole transition, whereas the Eu^{3+} $^5D_0 \rightarrow {}^7F_{2,4}$ is a forbidden electric dipole transition (parity selection rule). However, this selection rule can be related when Eu^{3+} is placed in a host lattice lacking in inversion symmetry such as Gd_2O_3 (Yang *et al* 2007). It is well known that cubic Gd_2O_3 lattice has C_2 or C_{3i} (or S_6) sites for rare earth doping (Blasse and Grabmaier 1994). Because the rare earth ion occupying C_{3i} site possesses a centre of inversion symmetry and the $^5D_0 \rightarrow {}^7F_{2,4}$ optical transition is strictly forbidden. Therefore, the dominant $^5D_0 \rightarrow {}^7F_{1,3}$ rare earth emission lines originate from forced electric dipole transitions of the ion occupying C_2 sites (where there is a lack of inversion symmetry) and from allowed magnetic–dipole transitions. Specifically, the forced electric dipole transitions for Eu^{3+} ($^5D_0 \rightarrow {}^7F_{2,4}$) are hypersensitive to the host crystallographic symmetry (Vetrone *et al* 2003). The Eu^{3+} ion occupies Gd^{3+} site in the doped Gd_2O_3 samples, resulting in the hypersensitive $^5D_0 \rightarrow {}^7F_2$ ($\Delta J = 2$) transition being the most prominent one in its emission spectrum. The intensity of the magnetic dipole transition ($^5D_0 \rightarrow {}^7F_1$) hardly changes with the crystal field strength around the Eu $^{3+}$ ion, while the intensity of hypersensitive electric dipole allowed transition ($^5D_0 \rightarrow {}^7F_2$) is highly sensitive to structural changes and environmental effects in the vicinity of the Eu^{3+} ions.

It is interesting to note that, the PL emission intensity of the nanorods is higher than that of the nanoparticles. In general, defects in materials come from quenching centres, which leads to non-radiative recombination and luminescence quenching (Abrams and Holloway 2004). Therefore, the difference in emission intensity should be mainly associated with the defects which come from surface states of the nanoparticles, because the recombination of electron–hole pairs due to surface defects is the most important pathway for non-radiative relaxation in nanoparticles. Thus the number of electron–hole pairs via non-radiative recombination in nanoparticles is less than that in nanorods. As a result, the

PL intensity of nanoparticles is lower than that of nanorods (Li *et al* 2010).

4. Conclusions

The cubic Gd_2O_3:Eu^{3+} nanoparticles and nanorods have been successfully synthesized by combustion and hydrothermal methods. PXRD measurements reveal that as-formed precursor and heat treated at 800°C for 3 h in combustion method gives mixed phase of monoclinic and cubic Gd_2O_3:Eu^{3+} and cubic dominant Gd_2O_3:Eu^{3+}, respectively. In the hydrothermal method as-formed product gives hexagonal $Gd(OH)_3$:Eu^{3+} and heat treated at 600°C for 3 h gives pure cubic Gd_2O_3:Eu^{3+} phase, respectively. The particle sizes for mixed phase (monoclinic and cubic) and cubic phases of Gd_2O_3:Eu^{3+} was found to be 48 nm and 34 nm, respectively. In the hydrothermal, diameter of the nanorods was found to be 15 nm and length varying from 50–150 nm. SEM micrographs of combustion method show fluffy in nature and in hydrothermal method tapered end nanorods with various sizes were observed. TEM results also confirm the particles and rods are in nanosize. In both the methods for cubic Gd_2O_3:Eu^{3+}, a dominant red emission at 612 nm was observed, which are promising for high performance display materials. The optical bandgap (E_g) in cubic Gd_2O_3:Eu^{3+} is ∼5.4 eV in both combustion and hydrothermal methods. However, in as-formed product mixed phase of monoclinic and cubic Gd_2O_3:Eu^{3+} and pure hexagonal $Gd(OH)$:Eu^{3+} phases, the bandgap is less when compared to cubic Gd_2O_3:Eu^{3+}.

Acknowledgements

The authors are grateful to TEQIP Lab of M. S. Ramaiah Institute of Technology, Bangalore, for providing facilities for preparation of materials. One of the authors (ND) acknowledges Management, Principal and HOD, B.M.S. Institute of Technology, Bangalore, for support and encouragement. (HN) thanks to Dr S C Sharma, Vice-chancellor, Tumkur University, Tumkur, for constant encouragement and support.

References

Abrams B L and Holloway P H 2004 *Chem. Rev.* **104** 5783
Blasse G and Grabmaier B C 1994 *Luminescent materials* (Berlin: Springer)
Cao H Q *et al* 2004 *Adv. Funct. Mater.* **14** 243
Chang C, Kimura F, Kimura T and Wada H 2005 *Mater. Lett.* **59** 1037
Dhananjaya N, Nagabhushana H, Nagabhushana B M, Chakradhar R P S, Shivakumara C and Rudraswamy B 2010 *Physica* **B405** 3795
Dhananjaya N, Nagabhushana H, Nagabhushana B M, Rudraswamy B, Shivakumara C and Chakradhar R P S 2011a *J. Alloys Compd.* **509** 2368
Dhananjaya N, Nagabhushana H, Nagabhushana B M, Rudraswamy B, Shivakumara C and Chakradhar R P S 2011b *Physica* **B406** 1639, 1645
Gu M, Liu Q, Mao S P, Mao D L and Chang C K 2008 *Cryst. Growth Des.* **8** 1422
Jis G, Liu K, Zheng Y, Song Y, Yang M and You H 2009 *J. Phys. Chem.* **C133** 6050
Klug P and Alexander L E 1954 in *X-ray diffraction procedure* (New York: Wiley)
Li L, Kyoung Yang H, Moon B K, Choi B C, Jeong J H and Kim K H 2010 *Mater. Chem. Phys.* **119** 471
Liu B, Gu M, Liu X, Ni C, Wang D, Xiao L and Zhang R 2007 *J. Alloys Compd.* **440** 341
Liu X, Zhou F, Gu M, Huang S, Liu B and Ni C 2008 *Opt. Mater.* **31** 126
Louis C, Bazzi R, Flores M A, Zheng W, Lebbou K, Tillement O, Mercier B, Dujardin C and Perriat P 2003 *Solid State Chem.* **173** 335
Nagabhushana B M 2008 Ph.D. Thesis, Bangalore University, Bangalore
Pan L K, Sunchang Q and Li C M 2004 *J. Phys. Chem.* **B108** 3404
Pires A M, Davolos M R and Stucchi E B 2001 *Int. J. Inorg. Mater.* **3** 785
Tang Q, Liu Z P, Li S, Zhang S Y, Liu X M and Qian Y T 2003 *J. Cryst. Growth* **259** 208
Vetrone F, Boyer J C, Capobianco J A, Speghini A and Bettinelli M 2003 *Chem. Mater.* **15** 2737
Williamson G K and Hall W H 1953 *Acta Metall.* **1** 22
Wood D L and Tauc J 1972 *Phys. Rev.* **B5** 3144
Xu A W, Gao Y and Liu H Q 2002 *J. Catal.* **207** 151
Yang J, Li C X, Cheng Z Y, Zhang X M, Quan Z W, Zhang C M and Lin J 2007 *J. Phys. Chem.* **C111** 18148